Journal of Solid State Chemistry 182 (2009) 2591–2597

Contents lists available at ScienceDirect

Journal of Solid State Chemistry

journal homepage: www.elsevier.com/locate/jssc

Synthesis and characterization of nanometric powders of UO_{2+x}, $(Th,U)O_{2+x}$ and $(La,U)O_{2+x}$

G. Rousseau [a,b,c,d], M. Fattahi [a], B. Grambow [a], L. Desgranges [b], F. Boucher [c], G. Ouvrard [c], N. Millot [d,*], J.C. Nièpce [d]

[a] Ecole des Mines de Nantes, SUBATECH, UMR 6457, 4, rue Alfred Kastler, BP 20722, 44307 Nantes, France
[b] CEA Cadarache, DEN/DEC/SA3C/L2EC, Bât. 315, 13108 Saint-Paul-les-Durance, France
[c] Institut des Matériaux Jean Rouxel, UMR 6502, 2, rue de la Houssinière, BP 32229, 44322 Nantes, France
[d] Institut Carnot de Bourgogne, UMR 5209 CNRS/Université de Bourgogne, 9 Avenue Alain Savary, BP 47870, 21078 Dijon cedex, France

ARTICLE INFO

Article history:
Received 24 March 2009
Received in revised form
23 June 2009
Accepted 24 June 2009
Available online 30 June 2009

Keywords:
Precipitation
Electrochemical reduction
Nanometric particles
UO_2
Powders characterization

ABSTRACT

This paper describes a new way of preparing nanometric powders of uranium oxide, to fit the needs of studies on UO_2 oxidation, through the electrochemical reduction of U(VI) into U(IV). These powders can also be doped with radionuclides if necessary. The precipitation of oxides occurs in reducing and anoxic conditions. This original method makes it possible to synthesize nanometric UO_2 powders with a calibrated size, as well as the Th- and La-doped UO_2 powders with a predefined composition. The powder characterization by the X-ray diffraction, X-ray photoelectron spectroscopy and transmission electron Microscopy shows the formation of spherical crystallites of UO_{2+x}, $(Th,U)O_{2+x}$ and $(La,U)O_{2+x}$ phases. The composition can be defined by the initial Th/(Th+U) and La/(La+U) ratios in solution and the particle size can be controlled by varying the pH.

1. Introduction

The oxidation of uranium dioxide has been studied for more than 50 years. It was first studied [1 and references therein] for fuel fabrication purposes and then later on for safety purposes to design a dry storage facility for spent nuclear fuel that could last several hundred years [2]. Therefore, knowledge of the changes occurring during the oxidation process is essential and a sound prediction of the behavior of uranium oxides requires an accurate description of the elementary mechanisms occurring on an atomic scale. Only the models based on elementary mechanisms should be able to provide a reliable extrapolation of laboratory results over timeframes spanning several centuries. The oxidation of UO_2 powders is usually partitioned in two stages: the first is associated with a pseudo-parabolic weight gain curve, while the second is associated with a sigmoid weight gain curve [3]. The pseudo-parabolic curve, attributed the formation of U_4O_9 and U_3O_7 on UO_2 powders, indicates a diffusion-controlled mechanism [4]. This mechanism was modeled with a finite difference algorithm [5] that was recently developed. The sigmoid curve is generally interpreted as the oxidation of U_3O_7 into U_3O_8 with a nucleation and growth mechanism [6]. This sigmoid curve is still a subject of debate in its quantitative interpretation. More precisely, the apparent activation energy for U_3O_8 formation deduced from the kinetic analysis of the experimental sigmoid curves, based on Avrami type laws, differs widely from 48 to 194 kJ mol^{-1} depending on the authors [6]. It was recently proven [7] that macro-cracking of the initial UO_2 sample changes the weight gain curves from which the apparent activation energy is deduced. Therefore, the actual activation energy of U_3O_8 can only be obtained on a sample unaffected by macro-cracking, i.e., powders with a grain size less than the critical size needed for macro-cracking [7–9]. The available industrial powders, obtained in dry or wet conditions, have an inhomogeneous grain size and are agglomerated. Moreover, some grains are stuck together and can be separated using oxidation by macro-cracking, which makes them unexploitable for a study on the U_3O_8 activation energy. Some UO_2 nanoparticles were recently produced by irradiating U(VI) solutions with electrons and γ-radiation [10], which yielded small particles with a narrow size distribution (22–35 nm). However, the powder did not consist of stoichiometric UO_2, but rather of a mixture of oxidation states: U(IV), U(V) and U(VI), with the likely existence of hydroxide or oxo-hydroxide phases, making them unusable for a proper study on UO_2 oxidation.

This paper describes an original method that can be used to synthesize UO_2 powders by the wet process, and thus avoid the drawbacks associated with industrial powders. The method is

* Corresponding author.
E-mail address:
nmillot@u-bourgogne.fr (N. Millot).

0022-4596/$ - see front matter © 2009 Elsevier Inc. All rights reserved.
doi:10.1016/j.jssc.2009.06.039

based on the electrochemical reduction of U(VI) into U(IV) and the precipitation of UO_2 in reducing and anoxic conditions at a constant pH. Moreover, the behavior of irradiated UO_2 depends on its radionuclide content, which means it is necessary to have radionuclide-doped UO_2 powders to reproduce the behavior of irradiated fuel. It will be shown that this technique can also be used to obtain UO_2 powders with different grain sizes and doped with tetravalent or trivalent elements [11,12].

2. Experimental

2.1. Starting solutions

All solutions were prepared with degassed Milli-Q water (Millipore, 18 MΩ cm) and all chemicals used were of analytical purity. Stock solutions of U(VI), Th(IV) and La(III) were, respectively, prepared by dissolving $UO_2(NO_3)_2 \cdot 6H_2O$, $Th(NO_3)_4 \cdot 4H_2O$ and $La(NO_3)_3 \cdot 6H_2O$ in 1 M NaCl. Different starting solutions with different Th/(Th+U) and La/(La+U) ratios were prepared from these stock solutions. The HCl and NaOH stock solutions were prepared in a glove box (MBraun, MB-200 with an extension model MB-200 MOD-E 1250/1000) under a nitrogen atmosphere, using the degassed water. The U(IV) stock solution was prepared in the glove box by electrolytic reduction of the initial U(VI) nitrate solution in the absence of O_2. The pH of this solution was kept below 1 to ensure the stability of U(IV). The U(IV) absorption spectrum was monitored periodically by a UV–vis spectrophotometer (Shimadzu, UV-2401PC) connected directly to the glove box by optical glass fibers (from 350 to 750 nm) capable of indicating a decrease in the U(IV) concentration with a sensitivity of 1%.

2.2. Synthesis method

All experiments were performed in a glove box under a nitrogen atmosphere for several days inside a reaction vessel containing 1 M NaCl (50–100 mL) at ambient temperature. The method is based on the electrochemical reduction of U(VI) into U(IV) using a galvanostat (Radiometer Voltalab 21), with the precipitation of UO_2, doped or not, occurring in reducing and anoxic conditions (N_2 bubbling) at a constant pH. Two synthesis methods were possible depending on the pH.

In the pH-range of 2.5–4, only UO_{2+x} and $(Th,U)O_{2+x}$ were studied. In fact, a previous publication showed that the precipitation of La(III) with UO_{2+x} only occurred for pH higher than 6 [13]. Therefore, an aliquot of the starting U(VI) or (U(VI)+Th) solutions were added to the NaCl solution under reducing conditions (Fig. 1). U(VI) was reduced electrochemically to U(IV) at a fixed pH and UO_{2+x} or $(Th,U)O_{2+x}$ precipitated. The pH increases due to the coulometric titration as compensated by the continuous addition of necessary quantities of the titration solution (HCl 0.1 M).

In the pH-range of 4–8, this method of synthesis did not lead directly to the precipitation of U(IV) solid phases, but first to the formation of schoepite or Na-polyuranates due to the high initial uranium concentration (0.005 m). Then the reductive dissolution of the U(VI) phases was too slow to allow for the formation of UO_2. In order to avoid U(VI) precipitation, the dissolved U(IV), or (U(IV)+Th(IV)), or (U(IV)+La(III) (0.03 M, pH < 1)) was, therefore, added slowly using an automatic burette (Titrino 718 STAT Metrohm), directly to the 1 M NaCl solution at the selected pH value (Fig. 2). The addition of this solution acidified the solution, which was counterbalanced by adding NaOH (0.1 mol/L) to keep the pH constant.

The stability of the reducing conditions in starting solutions, during both the test and sampling, was insured by various methods. Fig. 3 presents the solubility diagram of UO_2^{2+}/U^{4+} at 25 °C as a function of redox potential ($-5 < pe < 10$) for pH between 4.5 and 10 [14]. The redox potential, *pe*, is calculated from the measured potential, Eh, versus the normal hydrogen electrode (NHE) according to the following equation:

$$pe = \frac{E_h(\text{mV})}{59.2}$$

The solid phases controlling the solubility are also indicated. Based on this figure, it is necessary to ensure a reduction potential lower than −150 mV/NHE ($pe = -2.5$) in the pH-range of 5 to 9 to remain in the stability range of $UO_{2(cr)}$. This is indicated by the dotted line (Fig. 3). Hence, the redox potential Eh was fixed at −300 mV/N.H.E. In the pH-range of 2.5–4, the reduction potential was obtained by the UO_2^{2+}/U^{4+} equilibrium, making it possible to remain in the stability range of water.

Hence, all tests were run under permanent coulometric reduction conditions, which were ensured by two platinum electrodes (Radiometer Analytical). These electrodes were specially engineered for our experiment [11]. Because U(IV) readily oxidizes into U(VI) in the presence of O_2 both during the experiment and sampling, the removal of the oxygen traces of about 0.1 ppm in nitrogen gas was ensured using a redox cycle [11,15]. The nitrogen gas, containing oxygen traces (< 100 ppb) was splashed through a NH_4VO_3 solution containing a ZnHg amalgam. The vanadium solution was used as a color indicator. When the amalgam was no longer efficient, the violet vanadium (II) was oxidized by oxygen to form red–brown peroxovanadium cation. The purified nitrogen gas was then saturated with Milli-Q

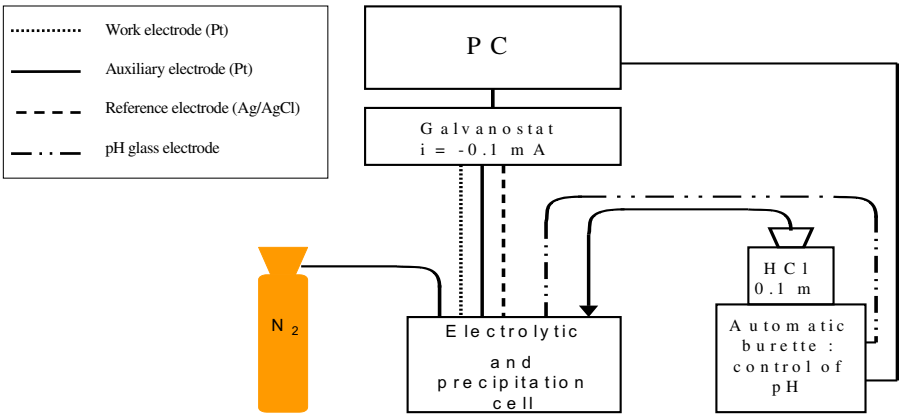

Fig. 1. Schematic diagram of the first synthesis method: UO_{2+x} and $(Th, U)O_{2+x}$ nanopowders obtained in the pH-range of 2.5–4.

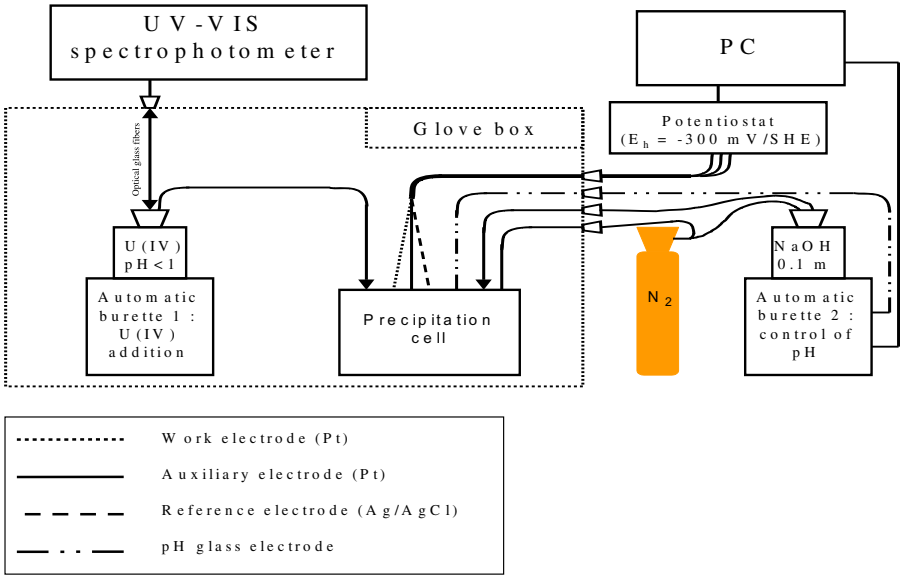

Fig. 2. Schematic diagram of the second synthesis method: UO_{2+x}, $(La,U)O_{2+x}$ and $(Th,U)O_{2+x}$ nanopowders obtained in the pH-range of 4–8.

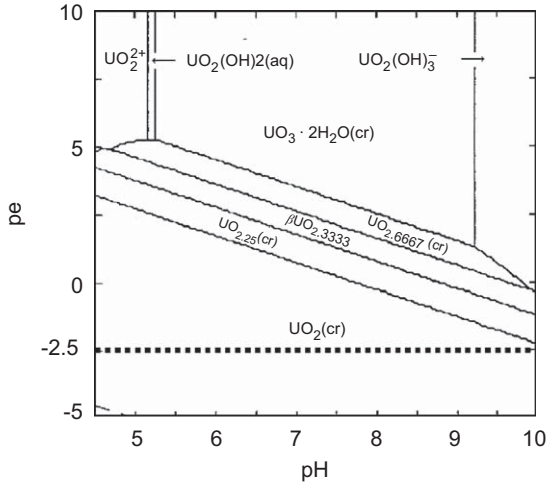

Fig. 3. Solubility diagram of UO_2^{2+}/U^{4+} at 25 °C as a function of redox potential ($-5 < pe < 10$), for a pH between 4.5 and 10. The solid phases controlling the solubility are indicated ($[U]_{tot} = 10^{-5}$ mol/L). The stability fields of the solid phases are indicated by the dashed lines. Dotted line indicates the minimum reduction potential −150 mV/N.H.E ($pe = -2.5$) to remain in the stability range of $UO_{2(cr)}$ in the pH-range of 5–9.

water and NaCl (1 M) before bubbling in the precipitation cell. The pH values were maintained constant (within ± 0.05 unit) with both synthesis methods using the above-mentioned burette. The pH values were measured continuously with a Metrohm combination glass electrode calibrated against NIST pH standard buffers. In order to keep the system as chemically simple as possible, N_2 bubbling makes it possible to maintain CO_2-free conditions during experiments.

Before introducing uranium, the pure 1 M NaCl solution was titrated coulometrically to reach a selected pH value and to remove any remaining traces of dissolved oxygen.

At the end of the experiments, the samples were filtered using a 0.22 μm filtrate, and the precipitates were washed twice with ultra-pure water to remove any NaCl traces prior to storage in the glove box.

2.3. Characterization of powders

X-ray diffraction (XRD) patterns of solid precipitates were obtained using two different diffractometers:

- an INEL diffractometer equipped with a curved position-sensitive detector (CPS 120 INEL) and monochromatic Co-$K\alpha_1$ X-rays ($\lambda = 0.17889$ nm) obtained with a primary focusing Ge monochromator,
- an INEL CPS120-equipped powder diffractometer set up in a horizontal Debye–Scherrer geometry using Cu $K\alpha_1$ radiation ($\lambda = 0.154056$ nm). In this case, Lindemann glass capillaries were used as sample holders.

The average coherent domain size was calculated from the broadening of the diffraction peaks using the Scherrer's equation.

High-resolution transmission electron microscopy (HRTEM) observations were made with a 200 kV cold-type field emission TEM (Hitachi HF 2000) equipped with a Gatan 666 multichannel spectrometer for electron energy loss spectroscopy (EELS) experiments. The experimental conditions led to an energy resolution of 0.9 eV full width at half-maximum (FWHM) for the zero loss peak. The energy dispersive X-ray (EDX) experiments were carried out with an X-ray detection system Kevex equipped with a Si/Li diode. The TEM was used to determine the structure of precipitates and particle size. The spot size was 60 nm, probe convergence semi-angle, $\alpha \approx 2.4$ mrad and inelastically scattered electrons were collected inside a semi-angle, $\beta \approx 50$ mrad.

Surface area measurements were performed using the BELSORP-mini II apparatus from Apollo Instruments with N_2 adsorbing gas. Samples (122 mg of powder) were outgassed at 398 K. The Brunauer–Emmett–Teller (BET) method was used to calculate the surface area from the isotherm of nitrogen adsorption. The mean apparent particle diameter of crystallites was inferred from the surface area based on the assumption that the nanometric crystallites were smooth and spherical with a narrow granulometric distribution.

The solid surface was also characterized by the X-ray photoelectron spectroscopy (XPS) (LHS 12 Leybold). Exposure to atmospheric oxygen was limited to the time necessary to transfer

the samples into the evacuated sample compartment. XPS spectra were obtained using the unmonochromatized Mg $K\alpha$ X-ray radiation source (1253.6 eV). The measured full-width at half-maximum peak height for the $Ag_{3d}^{5/2}$ band was (0.87 ± 0.03) eV. The energy scale of the spectrometer was calibrated using the following line positions in the noble metals: $Cu_{2p}^{3/2}$, 932.67 eV and $Au_{4f}^{7/2}$, 83.99 eV. The energy resolution was improved by reducing the pass energy to 31.5 eV.

3. Results of UO_{2+x} and $(Th,U)O_{2+x}$ synthesis with calibrated size

The solid phases were first characterized by the XRD. Fig. 4a shows the XRD diffractograms obtained from a UO_{2+x} solid precipitate at pH 2.5, while Fig. 4b shows those obtained from two $(Th,U)O_{2+x}$ solid precipitates at pH 2.5 with initial ratios Th/(Th+U) in solution of 0.1 and 0.5. All XRD diffractograms of the solid precipitates at pH <4 show several broad peaks indicating the formation of single fluorite UO_{2+x} or $(Th,U)O_{2+x}$ phases. Concerning UO_{2+x}, the average cell parameter was close to (0.5447 ± 0.0001) nm, which corresponds to the partly oxidized phase $UO_{2.19 \pm 0.01}$. Concerning $(Th,U)O_{2+x}$, the line broadening was too large to allow for an accurate determination of solids composition. In a previous publication, however [12], comparison between the lattice parameters obtained from our diffractograms and values calculated using the Cohen and Berman relationship for $(Th,U)O_{2+x}$ solid solutions based on the initial Th/(Th+U) ratios in solution showed that the lattice parameters obtained from our data were close to the calculated values. Hence, this suggests that crystalline $(Th,U)O_{2+x}$ phases are formed for this pH-range with a composition determined by the initial Th/(Th+U) ratio in solution. The line broadening indicates an average coherent domain size of about (12 ± 2) nm.

For pH values >3, the line broadening was too large to accurately determine the lattice parameter (Fig. 4b) due to the small particle size. Hence, transmission electron microscopy was preferentially used to characterize solid precipitates. At pH 6.5, the Scherrer's equation led to a coherent particle size range of 4–6 nm. The same solid phase was observed by HRTEM. Figs. 5a and b show that spherical nanocrystallites of UO_{2+x} are formed with a particle size between 4 and 6 nm, in agreement with XRD results. Moreover, the estimation of the lattice parameter gives (0.545 ± 0.005) nm from an average d_{111} interplanar distance of (0.315 ± 0.003) nm, which corresponds to an average composition of $UO_{2.11 \pm 0.02}$.

The BET surface area of this powder is equal to $(10.3 \pm 0.1)\ m^2\ g^{-1}$. This value is consistent with a moderately agglomerated powder, since the mean particle diameter deduced from this value is 53 nm, which is significantly higher than that obtained by both the XRD and TEM analysis. This difference is probably due to the sampling. Filtration tends to result in an agglomeration of the powders that are directly used for BET analysis, whereas these powders were dispersed for TEM characterization as seen in Fig. 5a.

Fig. 6 shows nitrogen adsorption–desorption isotherm of UO_{2+x} obtained at pH = 6.5. An adsorption step combining chemisorption and physisorption is revealed by this isotherm (first branch). This step is followed by a desorption step with physisorption only (second branch). The desorption branch

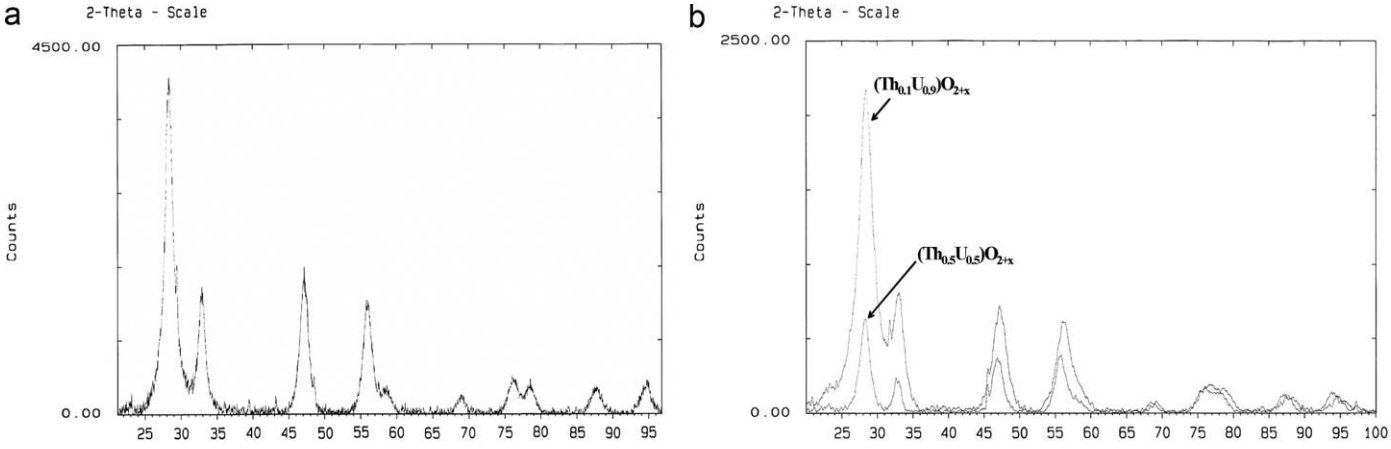

Fig. 4. XRD diffractograms: (a) UO_{2+x} and (b) $(Th,U)O_{2+x}$. $\lambda = 0.154056$ nm.

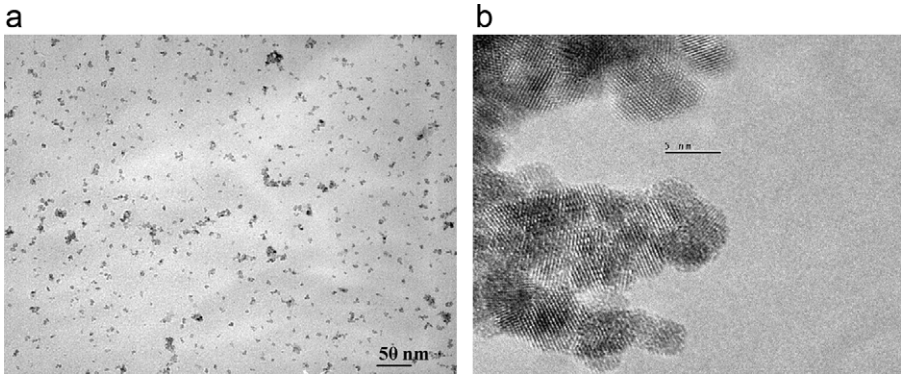

Fig. 5. HRTEM observation of UO_{2+x} powders obtained at a pH 6.5 (a) and (b).

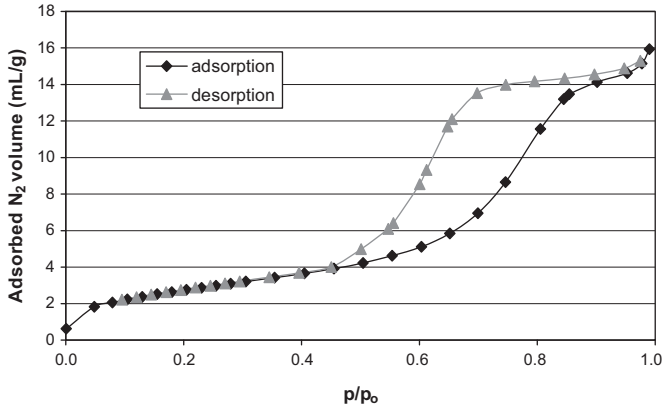

Fig. 6. Nitrogen adsorption–desorption isotherm of UO_{2+x} obtained at pH = 6.5. p/p_0 is the nitrogen relative pressure.

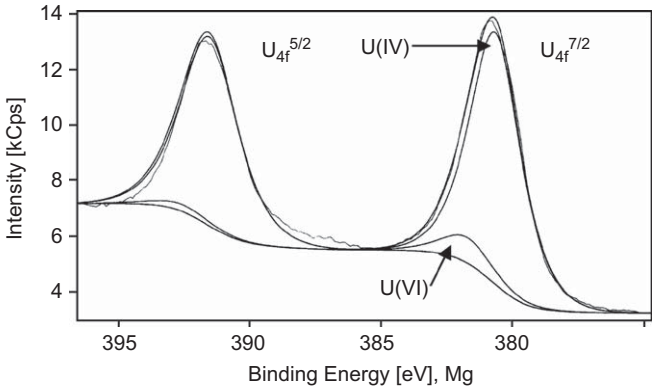

Fig. 7. $U_{4f}^{7/2}$ and $U_{4f}^{5/2}$ XPS peaks of UO_{2+x} obtained at pH 6.5. Typical deconvolution of U_{4f} has been realized: U(IV) and U(VI) contributions.

exhibits a IV-type shape in the IUPAC classification, associated with capillary condensation in mesopores. Below a p/p_0 relative pressure of about 0.4, the adsorption is characteristic of monolayer–multilayer adsorption. At higher relative pressure, capillary condensation in mesopores takes place, these pores should result of the nanograin stacking.

Finally, a quantitative analysis of the precipitates was conducted by XPS to determine the U(VI)/U(IV) ratio. In fact, U_{4f} bands are very sensitive to the chemical state of the uranium atom and the binding energies increase with the oxidation state [16]. For example, the $U_{4f}^{7/2}$ band occurs at ~379.9 eV in UO_2 and at ~381.6 eV in UO_3 [17,18]. As seen in Fig. 7, the $U_{4f}^{7/2}$ photoelectron line can be resolved into U(VI) and U(IV) components to determine their relative amounts [19]. The quantitative analysis of our precipitates gives an U(VI)/U(IV) ratio close to 0.10, which corresponds to an average composition $UO_{2.09\pm0.02}$. This value is in good agreement with the TEM-based calculation, and it appears that the composition of UO_{2+x} obtained in our experiments is close to $UO_{2.10\pm0.02}$.

Previous tests have shown that it is possible to produce very small uraninite crystallites of an average diameter of only 3 nm [20]. In order to allow for the formation of larger UO_2 particles, it was therefore necessary to add the acid U(IV) solution (about ~1–10 μl/min) at a very slow rate to decrease the nucleation rate of UO_2. In comparison, the grain size increases when the current decreases in the pH-range of 2.5 to 4, which corresponds to slower kinetics, which enhances grain growth [11,20]. It must also be pointed out that slower kinetics prevent the formation of schoepite or Na-polyuranates, the reductive dissolution of which is very slow before UO_2 formation.

In parallel, the average particle size decreases with an increasing pH, from 12 nm at pH 2.5 to 4–6 nm at pH 6.5. This demonstrates the influence of pH on the surface area. This observation is in good agreement with a study on the precipitation of nanoparticles in an aqueous medium [21].

Finally, the differences obtained for the O/U ratios are strong evidence that work should be conducted in an anoxic glove box to minimize the oxidation of UO_2 powders, which is known to be very fast even at 25 °C [22], particularly during the sampling and the characterization experiments.

4. Results of $(Th_yU_{1-y})O_{2+x}$ and $(La_yU_{1-y})O_{2+x}$ powders with defined compositions

The role of radionuclides – existing in the fuel after irradiation – needs to be taken into account, so as to study the oxidation kinetics of irradiated UO_2. Therefore, our precipitation method was used to synthesize UO_2 doped with radionuclides. The first tests were conducted with Th(IV) and La(III). Thorium may demonstrate homologous behavior to that of other tetravalent actinides (e.g. Np^{4+}, Pu^{4+} and Pa^{4+}) with respect to the ionic radius and ionic charge, whereas La is homologous to trivalent actinides (e.g. Pu^{3+}, Np^{3+}, Am^{3+} and Cm^{3+}) with respect to the ionic charge. The main difference between the behavior of Th(IV) and La(III) is due to their own intrinsic solubility. In a previous study, coprecipitation experiments showed clearly that their precipitation strongly depends on the pH [11]. Hence, the experiments were conducted in the pH-range between 2.5 and 9 for Th(IV) and 5 to 9 for La(III).

Stock solutions of Th(IV) and La(III) were prepared by dissolving both $Th(NO_3)_4 \cdot 4H_2O$ and $La(NO_3)_3 \cdot 6H_2O$ in 1 mol/L NaCl. The previous U(VI) solution was replaced by different starting solutions with different Th/(U+Th) and La/(U+La) ratios prepared from these stock solutions.

As observed for UO_{2+x}, XRD diffractograms cannot be used to accurately determine the composition/structure of solids due to the small particle size. Hence, transmission electronic microscopy was chosen to characterize solid precipitate.

Figs. 8a and b show the HRTEM observations obtained from UO_2 powders doped with Th(IV) and La(III), respectively. Contrary to the precipitation of amorphous $Th(OH)_4$(am) and $La(OH)_3$(am) in these conditions [11], spherical nanocrystallites were formed in presence of uranium in all cases, as was observed in the case of UO_{2+x}, while no amorphous phases were observed. Moreover, Fig. 8b shows that the interplanar distance, d_{111}, increases to 0.326 ± 0.007 nm, which is in good agreement with changes in the lattice parameter of $(La_yU_{1-y})O_{2+x}$ solid solution [23].

Moreover, a qualitative XPS analysis provided information on the environment of the atoms. This technique was used to analyze the surface of thoria–urania solid solutions during dissolution experiments [24]. Hence, the $Th_{4f}^{7/2}$ and $Th_{4f}^{5/2}$ bands for Th(IV) occurred at 335 and 344 eV, respectively. These energies are in good agreement with those of ThO_2, which indicate (Th–O) binding [25].

Fig. 9 shows the spectra of $La_{3d}^{5/2}$ and $La_{3d}^{3/2}$ obtained by XPS. These peaks are well defined and separated by 16.8 eV equal to the value given by Moulder [26]. Two contributions clearly appear on each peak separated by 3.9 eV. This signal is characteristic of (La–O) binding found in La_2O_3 [27,28].

Finally, in each case, the RN/(U+RN) ratios were quantified in the solid using EDX, combined with EELS and XPS for thorium and XPS only for lanthanum. All the Th/(U+Th) and La/(U+La) ratios determined in the solid were compared with the initial ratio in

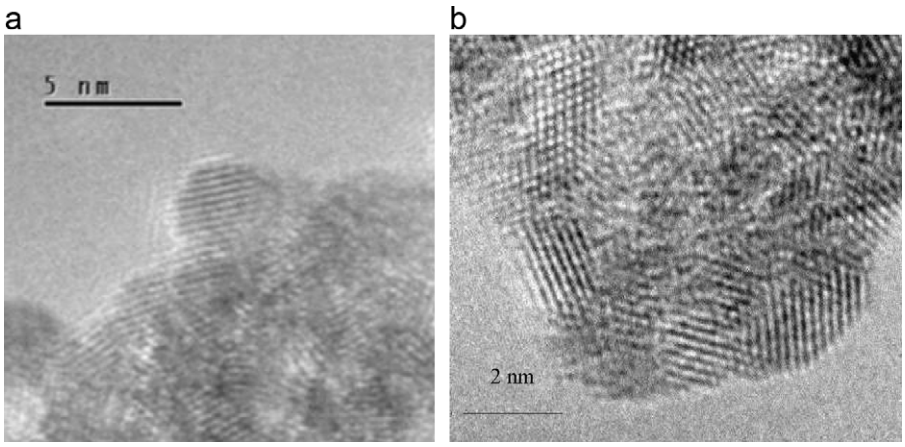

Fig. 8. $(Th_yU_{1-y})O_{2+x'}$ (a) and $(La_yU_{1-y})O_{2+x'}$ (b).

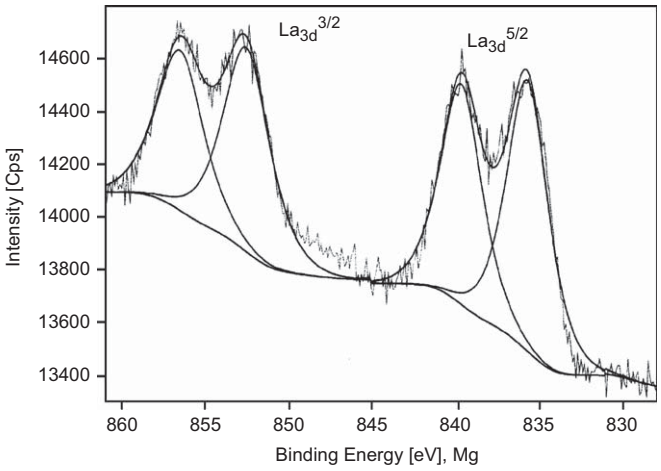

Fig. 9. $La_{3d}^{5/2}$ and $La_{3d}^{3/2}$ peaks obtained by XPS for $(La_yU_{1-y})O_{2+x'}$ obtained at pH 6.5.

solution of 0.126. The values show that the Th/(U+Th) and La/(U+La) ratios in the solid phase are close to those of the initial solution.

Hence, all these results show that our method can be used to synthesize Th- and La-doped UO_2 powders, with a defined composition corresponding to the initial ratio in solution. Moreover, these methods makes it possible to control the average particle size, which decreases with an increasing pH:

- from 4.5 nm at pH 6.1 to 3.5 at pH 7.7 and then to 2.7 at pH 8.2 for $(Th_yU_{1-y})O_{2+x'}$ and
- from 3.7 at pH 5.4 to 3.3 at pH 7.1 for $(La_yU_{1-y})O_{2+x'}$.

5. Conclusion

This paper describes a novel synthesis method for obtaining nanometric powders of UO_2 from aqueous solutions. The method is based on the electrochemical reduction of U(VI) into U(IV) and the precipitation of UO_2 in reducing and anoxic conditions at a constant pH. Powder characterization by XRD, XPS and TEM shows the formation of crystalline UO_{2+x} phases (fluorite structure), whose particle size can be controlled by varying the pH.

The resulting powders are suitable for studying U_3O_8 during UO_2 oxidation. Firstly, they do not contain any hydroxide or oxo-hydroxide phases which would modify the oxidation kinetics. Secondly, even if the powders are agglomerated, the agglomerate size (around 53 nm) is smaller that the critical size for macro-cracking (around 0.4 μm [7]), which means they should not exhibit any significant macro-cracking. In any case, their oxidation state is not $UO_{2.000}$. Even though a reducing heat treatment could be used to achieve UO_2 stoichiometry, the very high reactivity of UO_2 nanopowder to oxygen [1] prevents any accurate study of UO_2 oxidation in the vicinity of stoichiometry. This is why the formation of U_3O_8 should be studied by starting with an already pre-oxidized UO_2 nanopowder. Nevertheless, the physical and chemical state of the surface also can influence the formation kinetics of U_3O_8 [1,7]. In our case, the presence of water on the powder surface can have a significant impact. This point will be discussed in more detail following further study.

The proposed technique also makes it possible to obtain UO_2 powders doped with tetravalent and trivalent elements, whose average composition can be defined by the initial Th/(U+Th) and La/(U+La) ratios in solution. The coprecipitation of Th(IV) and La(III) with UO_2 always results in mixed and crystallized oxide $(Th_yU_{1-y})O_{2+x'}$ and $(La_yU_{1-y})O_{2+x'}$ precipitation. This approach seems relevant for simulating the influence of elements, such as fission products, in the irradiated fuel.

Acknowledgments

The authors would like to thank P. Moreau for his help with TEM analysis and V. Fernandez for his help with the XPS analysis. They would also like to thank Electricité de France (EDF) for its financial support as part of the PRECCI research program on long-term changes in CEA spent fuel waste packages. Finally, they would like to express their gratitude to Actinet for its financial support within the framework of the Joint Research Project called "Coprecipitation of radionuclides with UO_2 under anoxic and/or reducing conditions".

References

[1] R.J. McEachern, P. Taylor, J. Nucl. Mater. 254 (1998) 87.
[2] C. Ferry, C. Poinssot, C. Cappelaere, L. Desgranges, C. Jegou, F. Miserque J.P. Piron, D. Roudil, J.M. Gras, J. Nucl. Mater. 352 (2006) 246.
[3] G. Rousseau, L. Desgranges, F. Charlot, N. Millot, J.C. Nièpce, M. Pijolat, F. Valdivieso, G. Baldinozzi, J.F. Bérar, J. Nucl. Mater. 355 (2006) 10.
[4] R.J. McEachern, J. Nucl. Mater. 245 (1997) 238.
[5] A. Poulesquen, L. Desgranges, C. Ferry, J. Nucl. Mater. 367 (2007) 402.
[6] R.J. McEachern, J.W. Choi, M. Kolar, W. Long, P. Taylor, D.D. Wood, J. Nucl. Mater. 249 (1997) 58.
[7] L. Quémard, L. Desgranges, V. Bouineau, M. Pijolat, G. Baldinozzi, N. Millot, J.C. Nièpce, A. Poulesquen, J. Eur. Ceram. Soc. (2009) to be published 〈http://dx.doi.org/10.1016/j.jeurceramsoc.2009.04.010〉.

[8] J.C. Nièpce, G. Watelle-Marion, J. Mater. Sci. 13 (1978) 149.
[9] J.C. Nièpce, G. Watelle, J. Chim. Phys. 87 (1990) 1285.
[10] O. Roth, H. Hasselberg, M. Jonsson, J. Nucl. Mater. 383 (2009) 231.
[11] G. Rousseau, Coprecipitation of Th, Eu, La and Ac with UO_2 as Host Phase, University of Nantes, France, 2002 Thesis.
[12] G. Rousseau, M. Fattahi, B. Grambow, F. Boucher, G. Ouvrard, Radiochim. Acta 90 (2002) 523.
[13] G. Rousseau, M. Fattahi, B. Grambow, F. Boucher, G. Ouvrard, Radiochim. Acta 94 (2006) 517.
[14] I. Grenthe, J. Fuger, R.J.M. Konings, R.J. Lemire, A.B. Muller, C. Nguyen-Trung, H. Wanner, Chem. Thermodyn. Uranium. NEA. OECD 1 (1992).
[15] C. Alliot, B. Grambow, C. Landesman, J. Nucl. Mater. 346 (2005) 32.
[16] G.C. Allen, P.M. Tucker, J.W. Tyler, J. Phys. Chem. 86 (1982) 224.
[17] S. Sunder, N.H. Miller, W.H. Hocking, P.G. Lucuta, J. Alloys Compd 213/214 (1994) 503.
[18] S. Guilbert, M.J. Guittet, N. Barré, M. Gautier-Soyer, P. Trocellier, D. Gosset, Z. Andriambololona, J. Nucl. Mater. 282 (2000) 75.
[19] N.S. McIntyre, S. Sunder, D.W. Shoesmith, F.W. Stanchell, J. Vac. Sci. Technol. 18 (1981) 714.
[20] B. Grambow, R. Müller, C. Marquardt, P. Schubert-Bischoff, B. Luckscheiter, D. Schild, T. Bundschuh, H. Geckeis, Private Commun. (2001).
[21] L. Vayssières, Précipitation en milieu aqueux de nanoparticules d'oxydes. Modélisation de l'interface et contrôle de la croissance. Thesis, Université Pierre et Marie Curie, France, 1995.
[22] J.S. Anderson, L.E.J. Roberts, J. Harper, Chem. Soc. (1955) 3946.
[23] T. Fujino, C. Miyake, Handbook on the Physics and Chemistry of the Actinides, vol. 6, Elsevier, Amsterdam, 1991, p. 155.
[24] G. Heisbourg, S. Hubert, N. Dacheux, J. Purans, J. Nucl. Mater. 335 (2004) 5.
[25] C.D. Wagner, W.M. Riggs, L.E. Davis, J.F. Moulder, G.E. Muilenberg, Handbook of X-ray Photoelectron Spectroscopy, Perkin-Elmer, Eden Prairie, MN, 1979.
[26] J.F. Moulder, W.F. Stickle, P.E. Sobol, K.D. Bomben, Handbook of X-ray Photoelectron Spectroscopy. J. Chastain, R.C. Jr. King, Perkin-Elmer Corporation, 1992.
[27] Z. Zhang, W. Liu, Q. Xue, Wear 218 (1998) 139.
[28] A.M. De Asha, J.T.S. Critchley, R.M. Nix, Surf. Sci. 405 (1998) 201.